Simultaneous Detection of Multiple Magnetic Dipole Sources

Shuai Chang¹, Ye Lin¹, Yahong Rosa Zheng² , *Fellow, IEEE*, Xiaomei Fu¹

School of Marine Science and Technology, Tianjin University, Tianjin, 30072 China

Department of Electrical and Computer Engineering, Lehigh University, Bethlehem, PA 18015 USA

This paper proposes a new method to simultaneously estimate the locations and magnetic moments of multiple magnetic dipole sources without the prior knowledge of the number of dipoles in the 3D detection region. By initializing a large number of dipole sources evenly spaced in the detection region as potential candidates for the true dipoles, we introduce an indicator parameter for each dipole candidate, such that its Sigmoid function is the probability that the candidate converges to a true dipole. A joint optimization is then formulated to minimize the mean square of the regularized error between the measured magnetic gradients and the calculated gradients from the estimated dipoles. The proposed nonlinear optimization is solved by the Levenberg-Marquardt algorithm, yielding the indicators and their corresponding dipole locations and magnetic moments. The implementation details are also provided, such as using multiple initialization schemes to avoid local minima, selection of measurement points and candidate locations to avoid the "high-wall effect", and the need of preprocessing measurement data to avoid interference. Extensive simulations are conducted to investigate the effects of parameters, noise and interference on the detection performance, and the results show that the proposed algorithm is robust in different scenarios as long as the total number of measurements is larger than the total number of unknowns in the optimization problem. When the false alarm rate is set at 5×10^{-2} , the proposed algorithm achieves Recall of 0.91, 0.86, and 0.78 for the number of true dipoles being N=2,4,6, respectively, and the performance is robust against external interference and parameter selections.

Index Terms-multiple magnetic dipole detection, unknown dipole quantity, nonlinear optimization, high-wall effect.

I. INTRODUCTION

EFFECTIVE detection of magnetic sources has found important applications in underground and underwater object detection, vehicle tracking, navigation, and biomedical engineering [1]–[5]. Although magnetic sources in practice come with various shapes and sizes, a source can be treated as a dipole when the largest physical dimension of the source object is much smaller than the distances between the object and the measurement points [6], [7]. In most practical scenarios of magnetic sources, this condition is well satisfied and the dipole source assumption is usually adopted in practice.

Different from the active detection techniques that use either electromagnetic [8], [9] or acoustic signals, this research concerns the passive methods where the magnetic field is only passively measured in the receiver without active transmission. Therefore, simultaneous detection of multiple dipole sources becomes challenging because the magnetic fields of multiple sources are overlapped and field strength varies nonlinearly with the distance between the source and the measurement point. Separating the individual sources becomes a nonlinear deconvolution problem.

The methods of detecting a single dipole have been well developed in the past few decades [10]–[13]. A static dipole source has five independent gradient tensors and 3-D perpendicular measurements at more than two remote locations can usually solve for the 3D location coordinates, as well as the magnetic field strength and gradient tensor components. Yoshii [10] takes measurements from a fixed array of three

Manuscript received February 2020; revised July 2020; accepted July 13, 2020. Date of publication July 23, 2020; date of current version August 20, 2020. Corresponding author: S. Chang (email: shuai.chang@tju.edu.cn).

Color versions of one or more of the figures in this article are available online at http://ieeexplore.ieee.org.

Digital Object Identifier 10.1109/TMAG.2020.3011630

or four magnetometers, and computes the source location by solving the original high-order magnetic field and gradient models through transformation of unknowns and dimension reduction. Wynn [11] and Heath [12] propose a potential field inversion method to estimate the source location and magnetic properties from measurements of 3D magnetic gradients and Total Magnetic Intensity (TMI). The eigenvalues derived from TMI measurements are used to eliminate the ambiguous solutions due to nonlinearity. Reid [13] proposes a magnetic interpretation method in 3D using Euler deconvolution. This method is later improved in [14]-[16], where the 3D coordinates of the source dipole are solved directly using the relationship among the magnetic field vector, gradient tensor matrix and a structural index. The shortcomings of the Euler deconvolution method include the sensitivity to noises and the limitation that the 3D moments of the source cannot be estimated together with the coordinates. Teixeira [17] then adds an extra equation derived from eigen-analysis of the gradient tensor as a constraint to the solution of [14], and achieves better noise rejection.

The existing researches for detecting multiple dipole sources take three different approaches. The first approach is to generalize the single-source Euler deconvolution method to multiple-source situations by Hansen and Suciu [18]. This method requires taking high-order derivatives of the field, thus depending more on data quality. The second approach, as in [19] and [20], applies the Werner algorithm [19] to 3D multiple-source detection, which uses the thin-dike assumption to linearize the complex nonlinear magnetic field equations and leads to linear matrix inversion for deconvolution. Its advantage compared with the multi-source Euler deconvolution method is that the Werner method requires the first-order derivatives only regardless of the number of sources, thus has

lower noise sensitivity. However, the Werner deconvolution method is incapable of estimating the dip angle or susceptibility of the sources.

The third approach to multi-source detection uses nonlinear optimization which minimizes the mean square error between the measurements and the reconstructed magnetic field from the estimated source locations [21]-[23]. The Levenberg-Marquardt (LM) algorithm is often used to solve the nonlinear optimization, but the challenge is that the solution is easily trapped in local minima. Several methods have been utilized to solve the nonlinear optimization problem. He et al. [5] uses a set of random vertices to initialize the LM algorithm and calls it the random complex algorithm. Hu et al. [22] combines the hybrid of Particle Swarm Optimization (PSO) and the immune clone algorithm to provide an initial guess for the LM algorithm to search for the global optima. Hu et. al. [23] proposes another initialization method using the single-source Euler deconvolution method to estimate the initial locations of the dipole sources. For all these existing works, the number of sources is assumed to be known a priori and some also assume other prior knowledge about the sources, such as the magnetic moments or magnetization.

In this paper, we assume that the exact number of true dipole sources is unknown, but only an estimated maximal number of sources is available. We use a large number of initial dipole candidates and introduce a new indicator for each candidate. The Sigmoid function outputs of the indicators become the probabilities that the corresponding dipole candidate converges to a true dipole source. We then propose a new joint optimization method to solve for the 3D locations, magnetic gradients, and indicators of the dipole candidates by minimizing the mean squares of a regularized error between the measured and the estimated gradients from the candidates. The novelty of the proposed regularization term is that it encourages the nonlinear optimization to learn whether the candidates are true or false dipole sources while learning their locations and magnetic moments simultaneously.

The proposed nonlinear optimization problem is solved by the Levenberg-Marquardt algorithm with multiple initialization schemes to improve the chance of reaching the global optima. Through extensive simulations, we also discover the "high-wall effect" related to the measurement paths and selection of initial dipole candidates. The high-wall effect occurs when the measurement points form paths that separate the detection region into several sub-regions and if no initial candidates fall into the sub-region of a true dipole, then the cost function will increase along the measurement paths when some candidates try to pass the paths to converge to the true dipole. Therefore, the good strategy is to spread the initial candidates into every sub-region and it is easily incorporated in the random re-initialization step in the LM algorithm.

Extensive simulations are also conducted to evaluate the performance of the proposed algorithm under different parameters and noise/interference settings. To avoid underdetermined system solutions, the 5 independent gradient components are measured at each point in the detection region and the number of measurement points shall be no smaller than $7N_{\rm ini}/5$ with $N_{\rm ini}$ being the number of initial dipole candidates,

which is chosen to be slightly higher than the maximum number of true dipoles. The proposed algorithm achieves high rates of precision, recall, and accuracy when the number of initial candidates and/or the number of re-initialization sets increases. Meanwhile, the normalized mean absolute errors of the estimated locations and moments of the true positive dipoles also increase as the detection accuracy increases. The proposed algorithm is also robust against background noises and non-ambient interference such as other magnetic sources and live electrical wires. The proposed algorithm outperforms the existing multi-source detection algorithms [22], [23] even though the prior information such as the number of true dipoles and/or the magnetic moments of sources are kept unknown to the proposed algorithm but are fed to [22], [23]. We also investigate the effect of dipole approximation of real 3D sources and find that the performance degradation of the dipole approximation is negligible when the size of the sources is smaller than 10% of the distance between the measurement points and the sources.

II. PROBLEM STATEMENT

Let a magnetic dipole be placed at the origin of a Cartesian coordinate system. The magnetic field generated by the magnetic dipole at point (x, y, z) is calculated as

$$\boldsymbol{B} = \frac{\mu}{4\pi r^5} \begin{bmatrix} 3x^2 - r^2 & 3xy & 3xz \\ 3xy & 3y^2 - r^2 & 3yz \\ 3zx & 3yz & 3z^2 - r^2 \end{bmatrix} \boldsymbol{M} \quad (1)$$

where ${m B} = [B_x \ B_y \ B_z]^{\rm T}$ is the magnetic field vector, ${m M} = [M_x \ M_y \ M_z]^{\rm T}$ is the magnetic moment vector of the dipole, and $r^2 = x^2 + y^2 + z^2$. The permeability parameter is $\mu = \mu_r \cdot \mu_0$, where μ_r is the relative permeability of the medium, and $\mu_0 = 4\pi \times 10^{-7} {\rm T} \cdot {\rm m/A}$ is the magnetic permeability of the air. The magnetic gradient tensor matrix is then

$$G_{\mathbf{t}} = \begin{bmatrix} G_{xx} & G_{yx} & G_{zx} \\ G_{xy} & G_{yy} & G_{zy} \\ G_{xz} & G_{yz} & G_{zz} \end{bmatrix}$$

$$= \begin{bmatrix} \partial B_x / \partial x & \partial B_y / \partial x & \partial B_z / \partial x \\ \partial B_x / \partial y & \partial B_y / \partial y & \partial B_z / \partial y \\ \partial B_x / \partial z & \partial B_y / \partial z & \partial B_z / \partial z \end{bmatrix}$$
(2)

which contains only five independent components, because $G_{xy} = G_{yx}$, $G_{xz} = G_{zx}$, $G_{yz} = G_{zy}$, and $G_{xx} + G_{yy} + G_{zz} = 0$. If there are multiple dipole sources in a region, the magnetic field and gradient vector measured at a point in the region is simply the sum of the individual source measured at the point.

In real applications, \boldsymbol{B} and \boldsymbol{G}_{t} are usually available via measurements and the relationship between them and the relative positions of the sources are strongly nonlinear. To avoid the shortcoming that the magnetic field is easily polluted by environmental noises, we use only the five independent components of the gradient tensor in this research. If gradient is measured at J positions in a region, then the gradient vector has 5J elements

$$G = [G_1 \ G_2 \ ... \ G_j \ ... \ G_J]$$
 (3)

where $G_j = [G_{xx,j} \ G_{xy,j} \ G_{xz,j} \ G_{yy,j} \ G_{yz,j}]$ contains five independent gradient elements at the jth measurement point.

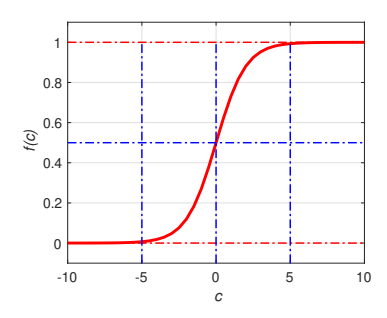


Fig. 1: Curve of the Sigmoid function.

Thereby, the problem of finding the locations and moments of the dipole sources is usually formulated as a minimum mean squared error problem

$$X^* = \underset{\mathbf{X}}{\operatorname{argmin}} [\mathbf{G} - \mathbf{g}(\mathbf{X})] [\mathbf{G} - \mathbf{g}(\mathbf{X})]^{\mathrm{T}}$$
 (4)

where X is the vector containing all the parameters of the dipole sources, and g(X) is the function for computing the gradient vector at the measurement points using the estimated X, and it is derived from (1) and (2). Assume the number of true dipole sources is N, then the commonly used parameters in X are

$$\boldsymbol{X} = [\boldsymbol{X}_1 \ \boldsymbol{X}_2, \cdots, \boldsymbol{X}_N] \tag{5}$$

and

$$X_n = [x_n, y_n, z_n, M_{x,n}, M_{y,n}, M_{z,n}], \quad 1 \le n \le N$$
 (6)

Obviously, the dimension of X increases linearly with the number of dipoles. The moments $M_{x,n}$, $M_{y,n}$ and $M_{z,n}$ can be randomly initialized without significant effect on optimization results. Note that most of the existing works [21]–[23] in dipole source detection assume that N is known a priori. However, this assumption maybe invalid in practice, and the optimization of (4) may result in poor estimation if the number of dipole sources is wrong.

III. NONLINEAR OPTIMIZATION METHOD

To avoid using the trial and error method to estimate the number of dipole sources, we propose a joint optimization method that simultaneously determines the number of dipoles and their related parameters. Let $N_{\rm ini}$ and $N_{\rm max}$ denote the initial guess and the possible maximum number of dipoles, respectively. Then the actual number of dipoles satisfies $N \leq N_{\rm max}$. Let $N_{\rm ini} \geq N_{\rm max}$, we construct a new parameter vector $\boldsymbol{X} = [\boldsymbol{X}_1, \cdots, \boldsymbol{X}_n, \cdots, \boldsymbol{X}_{N \rm ini}]$ where

$$\boldsymbol{X}_{n} = [x_{n}, y_{n}, z_{n}, M_{x,n}, M_{y,n}, M_{z,n}, c_{n}]$$
 (7)

The new parameter c_n is the input to the Sigmoid function which converts the parameter c_n into the probability that the nth candidate X_n is a true dipole source. The Sigmoid function, as shown in Fig. 1, is defined as

$$f(c_n) = \frac{1}{1 + e^{-c_n}} \tag{8}$$

with $c_n \in (-\infty, \infty)$.

Clearly, if $c_n > 5$, then $f(c_n) \approx 1$ indicating that the nth dipole candidate converges to a true dipole almost surely. If $c_n < -5$, then $f(c_n) \approx 0$ indicating that the nth candidate is a false source and shall be removed from the initial set. The Sigmoid function is globally differentiable and requires no constraints for c_n in the optimization problem defined later in (13). Also, the derivative of the Sigmoid is large when c_n is close to 0. This helps the LM algorithm which solves (13) converge fast.

One problem of using the new parameter set for the MSE minimization is that both the Sigmoid function and the moment vector M are linearly related with the magnetic gradients. This means that the two parameter sets $[M_{x,1}, M_{y,1}, M_{z,1}, c_1]$ and $[M_{x,2}, M_{y,2}, M_{z,2}, c_2]$ will produce the same gradient data when $[M_{x,1}, M_{y,1}, M_{z,1}] = u[M_{x,2}, M_{y,2}, M_{z,2}]$ and $f(c_1) = f(c_2)/u$, for u > 0. To avoid this problem, we propose a new objective function as

$$\Phi(\mathbf{P}) = ||[\varphi(\mathbf{P}_1), \cdots, \varphi(\mathbf{P}_j), \cdots, \varphi(\mathbf{P}_J)]||^2 \quad (9)$$

where $||\cdot||$ is the L2 norm of a vector, \mathbf{P}_j denotes the jth measurement point, and

$$\varphi(\mathbf{P}_j) = [\varphi_1(\mathbf{P}_j), \cdots, \varphi_k(\mathbf{P}_j), \cdots, \varphi_5(\mathbf{P}_j)]$$
 (10)

in which k indicates the kth independent gradient component measured at a point, and

$$\varphi_k(\mathbf{P}_j) = \left| G_{k,j} - \sum_{n=1}^{\text{Nini}} f(c_n) \cdot g_{k,j}(\mathbf{X}_n) \right| + \lambda \cdot |G_{k,j}| \cdot p(f(\mathbf{C}))$$
(11)

where $G_{k,j}$ is the kth component of the gradient vector G_j , and $g_{k,j}(X_n)$ is the computed gradient component generated by the nth estimated dipole at the jth measurement point. The vector $C = [c_1, c_2, \cdots c_{N \text{ini}}]$ is the collection of the indicators, λ is a positive constant set as 0.01 in this research, and p(f(C)) is a regularization term formulated as

$$p(f(C)) = \sum_{n=1}^{N_{\text{ini}}} f(c_n) \cdot (1 - f(c_n))$$
 (12)

Obviously, (12) is the sum variance of the Bernoulli variables $f(c_n)$, and the output of (12) will be 0 only when $f(c_n) = 0$ or 1 for all n. The regularization term encourages the optimization process to learn whether the dipole candidate is a true or false source. The dipole detection and estimation problem is formulated as

$$X^* = \operatorname*{argmin}_{\mathbf{X}} \Phi(\mathbf{P}) \tag{13}$$

The Levenberg-Marquardt (LM) algorithm is used to solve this nonlinear optimization problem. The LM algorithm is a widely used nonlinear least square algorithm and combines the advantages of gradient method and Newton method [24]. The nonlinear Least Squares problem in (13) has $7N_{\rm ini}$ unknowns, and the total number of independent gradient measurements is 5J. Therefore, the number of measurements shall satisfy $5J \geq 7N_{\rm ini}$ to ensure unique solutions.

Although it is common sense that the measurement points shall be uniformly spread in the detection region, the practical implementation may constrain the measurement points along

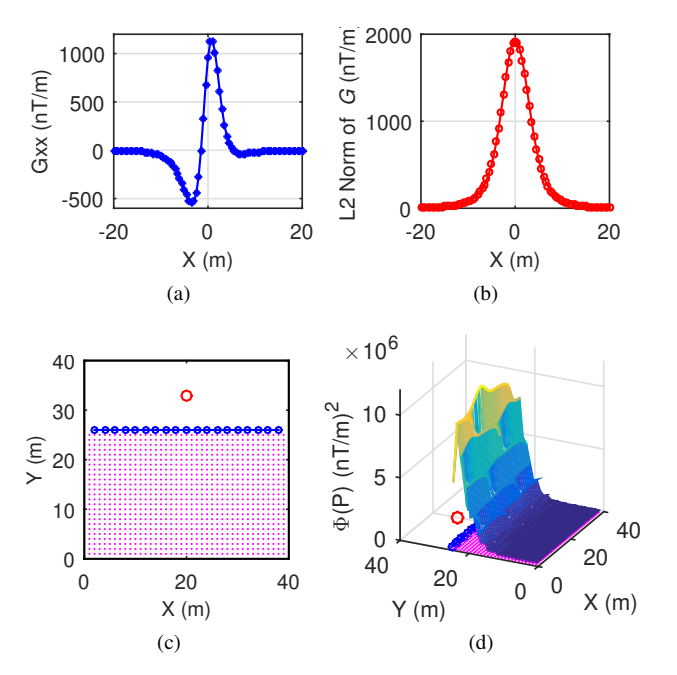


Fig. 2: Illustration of "high-wall effect". For (a) and (b), the dipole is located at (0,0,0) m and $M_x=M_y=M_z=2000 {\rm Am^2}$. The measurement points are spaced on a straight line from (0,0,5) m to (20,0,5) m. For (c) and (d), the red circle represents the true dipole at (20,35,0) m. The blue circles are measurement points. The red points represent the possible initial locations of the dipole candidates on the other side of the measurement path. The 3D surface in (d) indicates the values of (9) computed using the corresponding estimated dipoles.

some paths as is often done by vehicles. We discover through extensive simulations that, measurements aligning on a path may lead to a detrimental effect in solving (13). We call this the "high-wall effect" which occurs when the true dipole and initial dipole candidates are located on two sides of the measurement path. In this scenario, the cost function of the LM algorithm becomes very high as the locations of the estimated dipoles try to cross the measurement path to approach the true dipole location. The "wall" of the cost function is caused by the rapid increase of the computed magnetic gradient intensity. As the LM algorithm moves the estimates closer to the measurement point, the MSE increases rapidly and the LM algorithm would terminate without converging. The high-wall effect is demonstrated in Fig. 2.

If the measurement points form a line between the true dipole location and the initial locations of all the dipole candidates, then the dipole candidates have trouble to pass the line to reach the true dipole. This is because the estimated gradient intensity will increase and result in a large objective function (9). This conflicts with the minimum MSE principle and terminates the optimization without convergence. Thereby, the measurement points selected in the detection region shall avoid forming a closed loop. If the measurement paths divide the whole region into separate parts, then a sufficient number of dipole candidates shall be initialized in each of the divided sub-regions.

Algorithm 1 Joint Optimization of the Number of Dipoles and Their Parameters

Require:

Q – the number of dipole initialization schemes $(Q \ge 1)$; $N_{\rm ini}$ – the number of initial dipole candidates;

 $\mathcal{D} = \{\mathcal{D}^1, \mathcal{D}^2, \cdots, \mathcal{D}^Q\}$ – the Q sets of initial 3D positions of dipole candidates uniformly distributed in the detection area;

 $c_n = 5$ – initial indicators for $n = 1, \dots, N_{\text{ini}}$;

 $\alpha \in (0,1)$ – scaling factor for rejecting a solution; $\beta \in [0.4,1)$ – threshold for binary (true/false) decision;

1: **for** q = 1 : Q **do**

- 2: Select \mathcal{D}^q as the dipole initialization scheme, solve (13) using the Levenberg-Marquardt algorithm;
- 3: With the optimal X^* , estimate the (5J)-dimensional gradient vector $\hat{G} = [\hat{G}_1, \dots, \hat{G}_j, \dots, \hat{G}_J]$, where $\hat{G}_j = [\hat{G}_{xx,j}, \hat{G}_{xy,j}, \hat{G}_{xz,j}, \hat{G}_{yy,j}, \hat{G}_{yz,j}]^{\mathrm{T}}$;
- 4: Compute the L2 norm $||\Delta G||_2$ where $\Delta G = \hat{G} G$, and G is the measured gradients;
- 5: if $||\Delta G||_2 \le \alpha ||G||_2$ then
- 6: Accept the results of X^* , and set q = Q;
- 7: end if
- 8: end for
- 9: Remove all n in X^* whose coefficient $f(c_n) < \beta$;
- 10: Return X^* .

Another problem of the LM algorithm for nonlinear optimization is its no guarantee of global optima. Multiple runs of the LM algorithm with different initialization are often used to avoid local minima. Let the Q sets of magnetic dipole initialization schemes be $\mathcal{D}^q = \{ D_1^q, D_2^q, \cdots, D_{N \text{ini}}^q \}$, for $q=1,\cdots,Q$. The overall optimization method is summarized in Algorithm 1. The multiple initialization schemes used in the re-optimization process can help make better approximation to the true dipoles, and lead to better optimization results. Although this approach means high computational complexity, the multiple runs with different initialization schemes can be highly parallel. The resulting cost functions are compared and the lowest one is accepted as the global optimal solution.

IV. SIMULATIONS AND ANALYSIS

In the simulation experiments, we set a round space of 20 m radius as the detection region. Up to six magnetic dipoles are contained in the space, that is $N \leq 6$. The dipoles distribute randomly in this area with their height $z_n = 0$. Their moments are randomly selected from Table I and they are different from each other.

TABLE I: MAGNETIC MOMENTS OF THE DIPOLES

No.	$M_x \; (\mathbf{A} \cdot \mathbf{m}^2)$	$M_y \; (\mathbf{A} \cdot \mathbf{m}^2)$	$M_z \; (\mathrm{A} \cdot \mathrm{m}^2)$
1	1000	2000	1000
2	2000	1000	2000
3	1000	2000	2000
4	2000	1000	1000
5	2000	2000	1000
6	1000	1000	2000

Six different situations with N=1:6 are considered. The parameters of the optimization algorithm are set as: $N_{\max}=6$; $N_{\min}=9$; for $n=1,\cdots,N_{\min}$, randomly select $M_{x,n},M_{y,n},M_{z,n}\in[0,3000]\mathrm{Am^2}$, and the initial locations of dipoles are set such that x_n and y_n are evenly spread on the X-Y plane of radius R=20 m and $z_n\in[-5,5]$ m are randomly selected. The number of measurement points is selected as J=17. An independent white Gaussian noise is added to each measurement. The noise distribution is $\mathcal{N}(\mu,\sigma^2)$ with the mean $\mu=0$ nT/m and the standard deviation $\sigma=0.5$ nT/m. The measurement points and two initialization schemes are shown in Fig. 3 as an example.

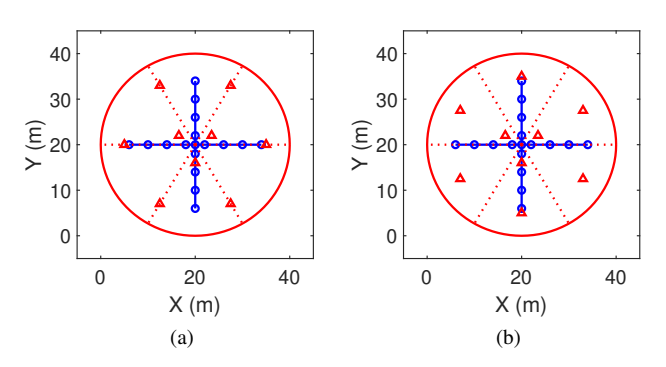


Fig. 3: Two initialization schemes for Algorithm 1. The small blue circles represent the J=17 measurement points projected on the plane of z=5 m. The red triangles are the initial locations of (x_n,y_n) , and the big red circle shows the detection region.

For each experimental case, we run 500 random trials and collect statistics. The first metric is the percentage of successful trials, or the number of trials that results in a valid solution of X^* divided by the total number of trials. The second type of metrics are related to true positive, false positive, and false negative dipoles in the resulting X^* . The 3D locations of the detected dipoles in X^* are compared with the ground truth dipoles generated in the simulation. Let the Euclidean distance between a detected dipole n and a true dipole j be $d_{n,j}$. For each n in X^* , if $d_{n,j} < \delta$ exists for some j, then the nth dipole is a true positive detection. If $d_{n,j} > \delta$ for all j, then the nth dipole is a false positive detection. For each true dipole j, if there is no detection n that satisfies $d_{n,j} < \delta$, then a false negative is counted for the jth true dipole. The threshold is set to $\delta = 0.4$ m in this study.

We use $N_{\rm tp}$, $N_{\rm fp}$ and $N_{\rm fn}$ to represent the numbers of "true positive". "false positive" and "false negative" dipoles, respectively. Let $N_{\rm total}$ be the number of total true dipoles, then $N_{\rm total} = N_{\rm tp} + N_{\rm fn}$. Since we remove the negative detection in Algorithm 1, we only concern the positive decisions and ignore the true negatives. The commonly used three indexes, Precision, Recall, and Accuracy, are defined as

$$Precision = N_{tp}/(N_{tp} + N_{fp})$$

$$Recall = N_{tp}/(N_{tp} + N_{fn})$$

$$Accuracy = N_{tp}/(N_{tp} + N_{fn} + N_{fp})$$
(14)

Note Precision is the true positive prediction rate of the detection algorithm. Higher Precision means that the

TABLE II: VALUES OF PARAMETERS

parameters	values
\overline{Q}	1, 2, 3, 4, 5, 6
α	0.01, 0.03, 0.05, 0.07, 0.09
β	0.4, 0.5, 0.6, 0.7, 0.8, 0.9
N	1, 2, 3, 4, 5, 6
$N_{ m ini}$	4, 5, 6, 7, 8, 9, 10, 11

detection algorithm has a higher level of trust. *Recall* is the true detection rate, or sometimes also called the sensitivity. A good detection algorithm often achieve both high *Precision* and high *Recall*. *Accuracy* is simply a ratio of correctly detected dipoles to all results.

The third type of metrics is for the true positive detection. The mean relative absolute errors (MRAE) of the positions and moments between the detected dipoles and the true dipoles are defined as

$$MRAE_{Pi} = MAE_{Pi}/R$$

$$MRAE_{Mi} = MAE_{Mi}/|M_i|$$
(15)

where i is either x, y or z, MAE is the mean absolute error, $|M_i|$ is the magnitude of the magnetic moment of the true dipole, and R is radius of the detection region.

A. Influence of Parameters

Extensive simulations are conducted according to Table II to test the influence of the parameters Q, α and β in Algorithm 1, the number of true dipoles N, and the number of initial dipoles $N_{\rm ini}$.

First of all, to show the effectiveness of multiple initialization schemes and re-optimization in Algorithm 1, the number of initialization sets Q is selected from 1 to 6. The other parameters are fixed as $\alpha=0.03,\ \beta=0.5,\ N_{\rm ini}=9$. The detection results with N=4 is shown as an example in Fig. 4. It can be seen that the value Q has a big impact on the number of trials that can yield an acceptable solution, as well as the Recall and Accuracy of the detection. This reveals that Q>1 can help improve the convergence of the LM algorithm. Very little change can be found in Precision, position errors, and moment errors.

Next, the relationship between the detection performance and number of true dipoles is studied. Six situations that N=1 to 6 are considered under the conditions that Q=3, $N_{\rm ini}=9,~\alpha=0.03,~{\rm and}~\beta=0.5.$ The detection results are shown in Fig. 5. The percentage of good trials decreases as Nincrease, as shown in Fig. 5(a). This is for the obvious reason that more dipoles require more resources such as Q, J, and $N_{\rm ini}$ to achieve better performance. Similar to the percentage of good trials, the *Recall* and *Accuracy* also decrease with N, as shown in Fig. 5(b), while Precision drops initially from N = 1 to N = 2 but remains unchanged when Nincreases beyond 2. Similar degradation is observed in the error of location estimation as shown in Fig. 5(c), but the error of moment estimation remains more or less the same as N increases. This means that the moment estimation is consistent once the detection is correct.

Next the influence of $N_{\rm ini}$ is studied with $N_{\rm ini}$ varying from 4 to 11. Other parameters are fixed as $Q=3,~\alpha=0.03,$

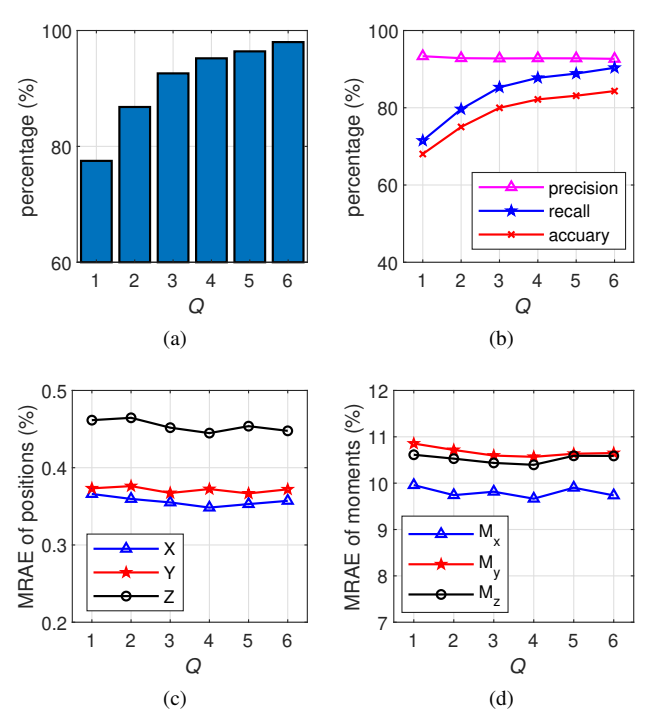


Fig. 4: Comparison of detection performance under different Q values. (a) Percentage of good trials yielding acceptable solution; (b) Precision, Recall and Accuracy; (c) MRAE of dipole positions; (d) MRAE of magnetic moments.

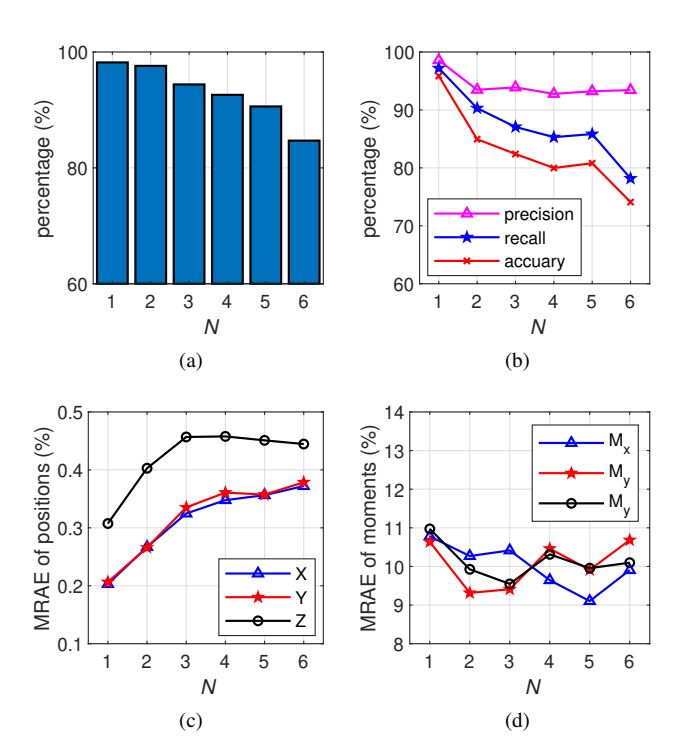


Fig. 5: Comparison of detection performance under different N. (a) Percentage of good trials yielding acceptable solution; (b) Precision, Recall and Accuracy; (c) MRAE of dipole positions; (d) MRAE of magnetic moments

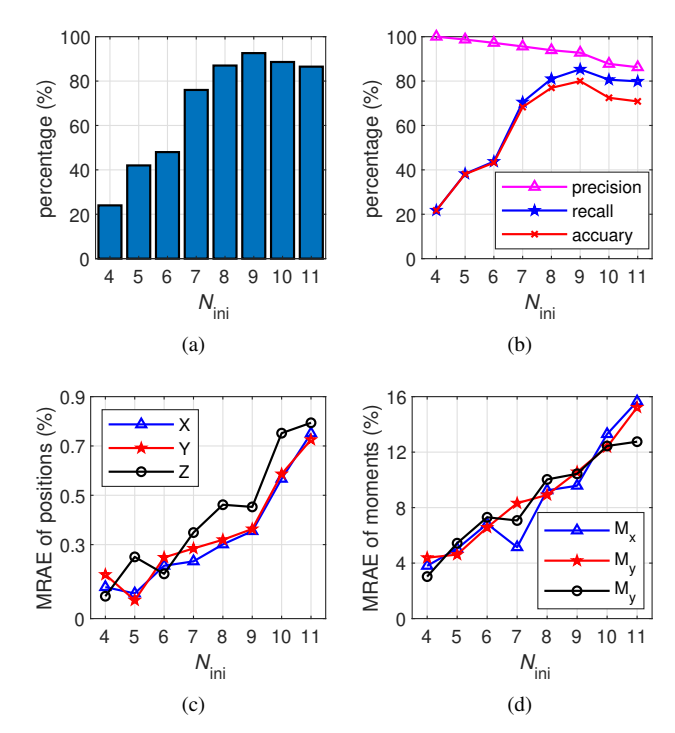


Fig. 6: Comparison of detection performance under different $N_{\rm ini}$. (a) Percentage of good trials yielding acceptable solution; (b) Precision, Recall and Accuracy; (c) MRAE of dipole positions; (d) MRAE of magnetic moments.

 $\beta=0.5$, and N=4. Detection results are shown in Fig. 6. The percentage of good trials, Recall, and Accuracy increase quickly when $N_{\rm ini}$ changes from 4 to 9 and then decrease slightly when $N_{\rm ini}$ increases further from 9 to 11, as seen in Fig. 6 (a) and (b). However, Precision decreases slightly with the increase of $N_{\rm ini}$. The estimation errors of detected dipoles also increase with $N_{\rm ini}$, as shown in Fig. 6(c) and (d). These results indicate that the selection of $N_{\rm ini}$ has a sweet spot that is around 2N. For this example of N=4, the good values are $7 \leq N_{\rm ini} \leq 9$. Without the prior knowledge of N, it is better to select a larger $N_{\rm ini}$ than a smaller one.

To test the influence of the scaling factor α on the detection results, α is varied from 0.01 to 0.11 with a step size of 0.02, while other parameters are fixed. The results for Q=3, $\beta=0.5$, and N=4 are taken as an example, shown in Fig. 7. As a larger α value accepts the optimization results with larger errors, the percentage of good trials increases with α , so do Recall and Accuracy. In contrast, Precision, along with the MRAEs, decreases with α , because large optimization errors lead to "false positive" and "false negative" dipoles, as well as large estimation errors in "true positive" dipoles.

Furthermore, the influence of threshold β is tested with values varying from 0.4 to 0.9. We set $\alpha=0.03,\ Q=3$ and N=4. Detection results are illustrated in Fig. 8. As β is used to select dipoles from accepted trials, it has no effect on the number of accepted trials. A higher β results in better Precision and slightly dropped Accuracy and Recall, as shown in Fig. 8(b). The location estimation errors remain pretty constant with β while the moment estimation errors

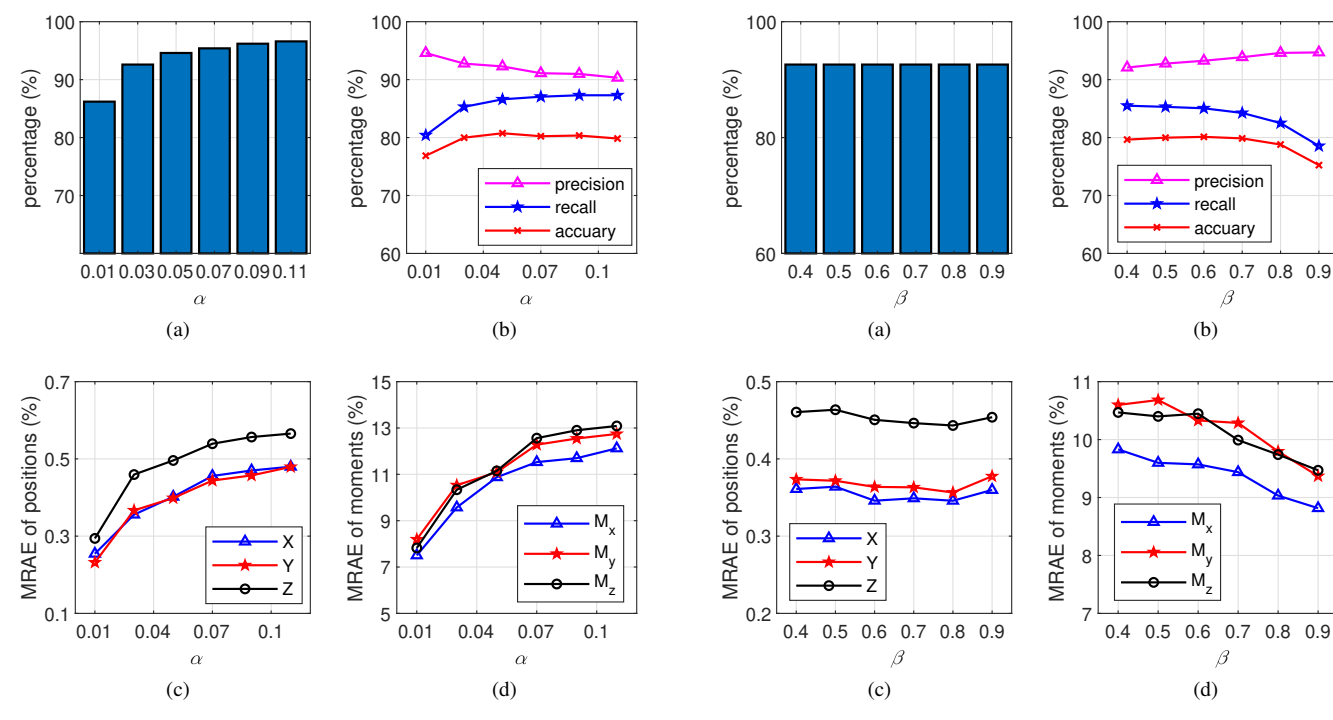


Fig. 7: Comparison of detection performance under different α values. (a) Percentage of good trials yielding acceptable solution; (b) Precision, Recall and Accuracy; (c) MRAE of dipole positions; (d) MRAE of magnetic moments

Fig. 8: Comparison of detection performance under different β values. (a) Percentage of good trials yielding acceptable solution; (b) Precision, Recall and Accuracy; (c) MRAE of dipole positions; (d) MRAE of magnetic moments

reduce as β increases, as shown in Fig. 8(c) and (d). This means that increasing β will reject more candidates that are close to the true dipoles but have different magnetic properties. This makes β a good quality control parameter.

Last, we evaluate the relationship between the conflicting goal of increasing true positive and reducing the false positive detection. Let $R_{\rm fp}=N_{\rm fp}/N_{\rm total}$. We set parameters Q=3, $\alpha=0.03$, $N_{\rm ini}=9$, N=2,4 and 6. Varying the detection threshold β yields a series of Recall, and the corresponding R_{fp} is computed. Fig. 9 shows the Recall versus $R_{\rm fp}$ plot, where at the false alarm rate of 5×10^{-2} , the proposed algorithm achieves Recall of 0.91, 0.86, and 0.78 for N=2,4,6, respectively. The best performance configuration is at the top left corner where Recall is high and $R_{\rm fp}$ is relatively low.

B. Sensitivity to Measurement Noise and Interference

Three kinds of measurement noise and interference are added to the simulation to test the sensitivity of the proposed method. We used $N=4,\,n_{\rm ini}=9,\,Q=3,\,\alpha=0.03,\,\beta=0.5$ and ran 500 trials. The magnetic moments of the true dipoles were randomly selected from Table I.

First, different levels of white Gaussian noises are added to the gradient measurements. With $\mu=0$ and σ varying from 0.5 to 15, the signal-to-noise ratios (SNR) of the measured gradient vectors corresponded to 55.5 dB to 25.5 dB. Detection results are shown in Fig. 10.

Second, we evaluate the influence of non-target interference in the detection region. Let $N_{\rm d}$ denote the number of non-target magnetic interference sources. The magnetic moment

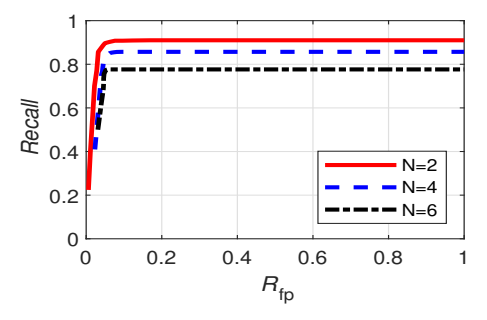


Fig. 9: Recall vs. R_{fp} for N = 2, 4 and 6.

components of the non-target dipoles were randomly selected from $[50,300] \mathrm{Am^2}$. The white Gaussian noise was fixed as $\mathcal{N}(0,0.5^2)$. Detection results are shown in Fig. 11 for six situations where $N_{\mathrm{d}}=1:6$.

Third, we evaluate the interference from live electrical wires in the detection area. The center of the detection region is at (20,20,0) m. Two straight wires pass through the detection region linking random points in the region. Specifically for our simulation, wire 1 passed through (25,-5,0) m and (35,45,0) m, and wire 2 passed through (-5,8,0) m and (40,42,0) m. The current intensities varied as I=1 to 17 A with a step size of 2 A. The magnetic field generated by the wires were added to the measurement points. Detection results are shown in Fig. 12.

In all the three scenarios, the position and moment errors of the detected targets show obvious increase with the increase

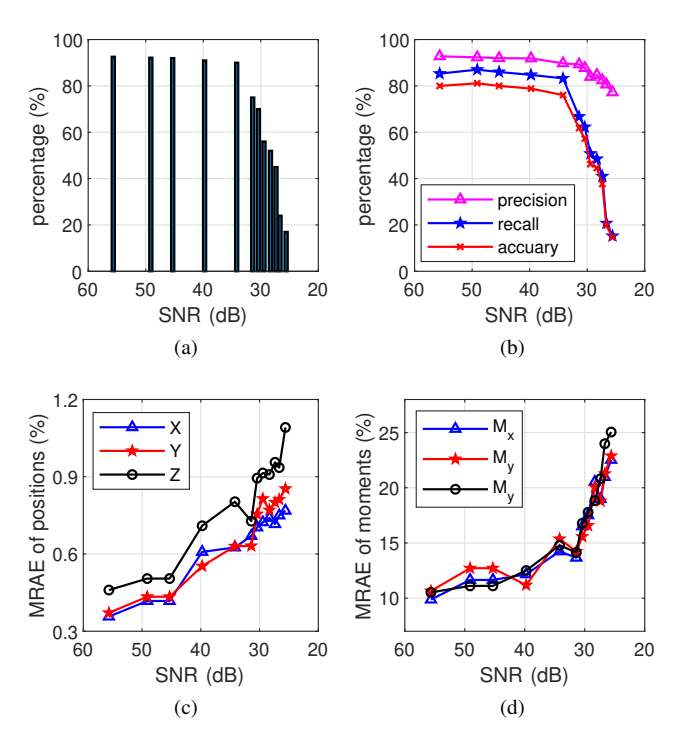


Fig. 10: Effects of white Gaussian noise. (a) Percentage of good trials yielding acceptable solution; (b) Precision, Recall and Accuracy; (c) MRAE of dipole positions; (d) MRAE of magnetic moments.

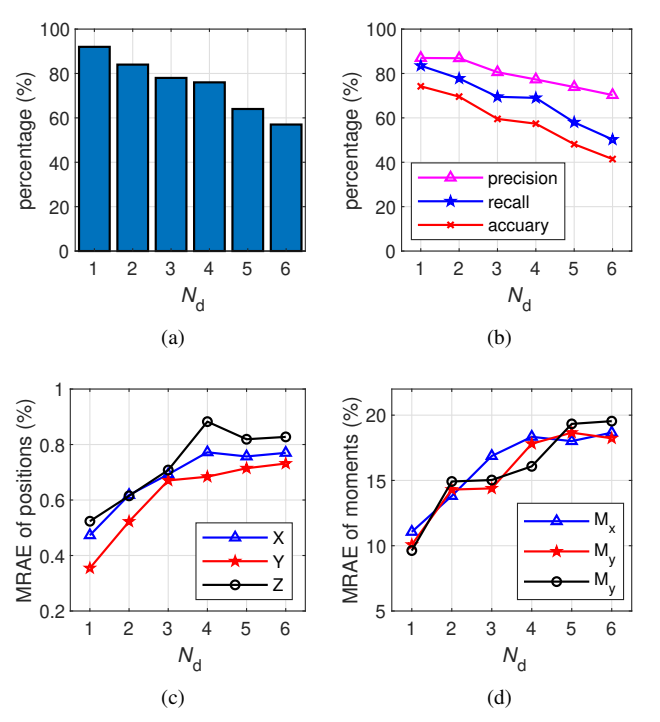


Fig. 11: Detection performance under different levels of noise from non-target dipoles. (a) Percentage of good trials yielding acceptable solution; (b) Precision, Recall and Accuracy; (c) MRAE of dipole positions; (d) MRAE of magnetic moments.

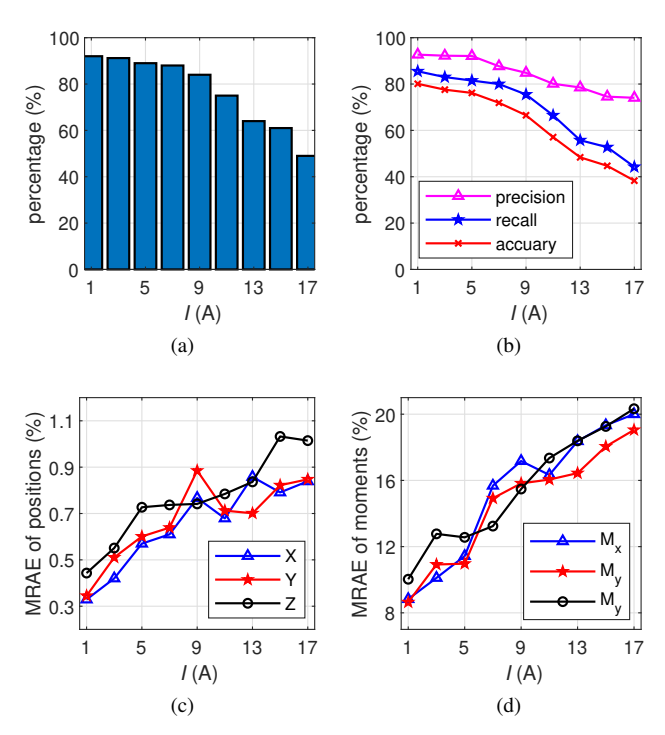


Fig. 12: Detection performance under different levels of electromagnetic noise. (a) Percentage of good trials yielding acceptable solution; (b) Precision, Recall and Accuracy; (c) MRAE of dipole positions; (d) MRAE of magnetic moments.

of noise intensity or the number of noise sources. For the first scenario of white Gaussian noises, the proposed method shows good robustness when SNR is higher than 34 dB $(\sigma \approx 6)$, and then the performance is declined rapidly when noises become stronger. For the second scenario of nontarget dipole interference, Precision, Recall and Accuracy show downward trend because the non-target dipoles are very easily detected as "false positive" when they are located near the measurement points. If the interfering sources are far away from the measurement points, the their magnetic field strengths act more like the white noises and reduce detection performance. For the third scenario of live wires passing through the detection region, the electromagnetic field strength is proportional to the current intensity and inversely proportional to the distance between the wires and the measurement points. The results show good robustness of the proposed method when the current increases from 1 to 9 A, but the performance worsens quickly when the current increases beyond 9 A. This reveals that the nearby underground or aerial cables with strong currents may severely decrease the detection performance. However, as the live wires exhibit spatial structure, their effect can be detected easily and some data preprocessing methods, such as method of moments [25] and finite element method can be employed to compute and remove the interference before applying the proposed method.

C. Evaluation of Dipole Approximation

To verify the effectiveness of dipole approximation for true objects, we used four spherical and four cylindrical magnetic objects as targets to generate the measurements. The radius of spherical objects is 0.15 m. The radius and length of the cylindrical objects are 0.1 m and 0.4m, respectively. In two situations, the geometric centers of these objects are randomly placed on the z=0 plane in the detection region. The objects are uniformly magnetized with 1.5×10^5 m/A. The gradient vectors are computed using the finite element method for the 17 measurement points. White Gaussian noises are also added with SNR = 49 dB. The optimization method used the dipole approximation to reconstruct the gradient vectors and used the parameters Q=3, $\alpha=0.03$, $\beta=0.5$, and $N_{\rm ini}=9$. Statistics of 500 trials are listed in Tables III and IV, where results of ideal dipole sources are compared.

TABLE III: Precision, Recall and Accuracy WITH DIFFERENT MAGNETIC OBJECTS

Object	Precision(%)	Recall(%)	Accuracy(%)
Sphere	90.9	85.8	78.9
Cylinder	89.7	83.7	76.3
Ideal Dipole	92.0	87.0	81.1

TABLE IV: ESTIMATED POSITION ERROR WITH DIFFERENT OBJECTS

Object	$MRAE_{Px}(\%)$	$MRAE_{Py}(\%)$	$MRAE_{Pz}(\%)$
Sphere	0.5853	0.5702	0.6701
Cylinder	0.6401	0.7015	0.7635
Ideal Dipole	0.4175	0.4340	0.5045

In addition, the estimated object locations are plotted with the true target locations in Fig. 13(a) and (b). These locations were used to compute the total magnetic field intensity ||B|| and two gradient components G_{xy} and G_{xz} for the 17 measurement points, as shown in Fig. 13(c) and (d).

The results in Tables III and IV and Fig. 13 demonstrate that both the spherical and cylindrical types of objects can be well detected using the dipole approximation. The performance of spherical objects is closer to that of the ideal dipole because the geometric features of a spherical magnetic object are better approximated by the ideal dipoles than the cylindrical objects. Nevertheless, both types of objects are well detected using the ideal dipole approximation.

D. Some Typical Scenarios and Detection Results

Typical cases with correct detection results are illustrated in Fig. 14 for N=2,4,6. The true dipoles and detection results are represented by small red circles and black stars, respectively. The small triangles represent the initial locations of the $N_{\rm ini}$ dipole candidates.

In contrast, Fig. 15 shows examples of miss detection or "false negative" for N=4 under the conditions that Q=3, $\alpha=0.03$ and $\beta=0.5$. Fig. 15 (a) shows an example of true dipoles, detected dipoles, and initial candidates. Fig. 15 (b) shows all the "false negative" dipoles in the accepted results from 500 trials. It is obvious that most of the "false

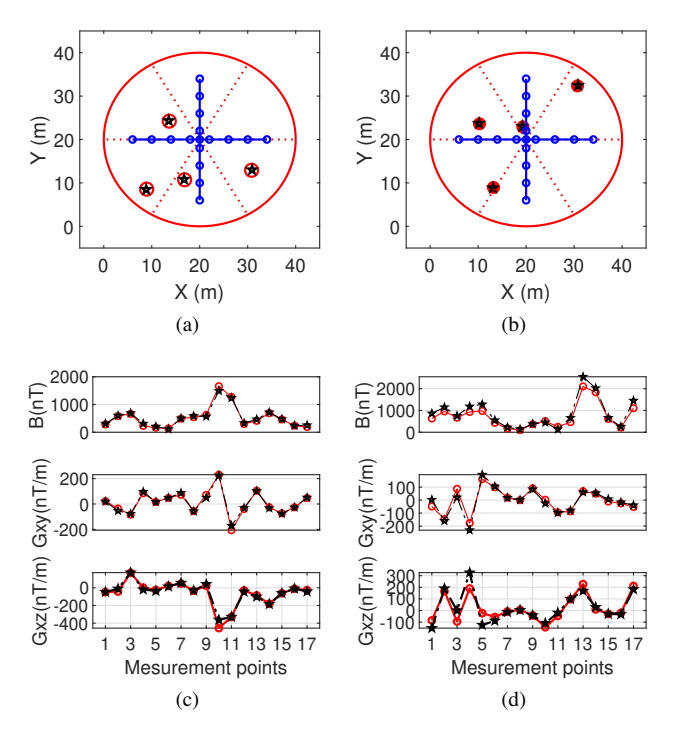


Fig. 13: Detection results of dipole approximation. Legends: red circles – ground truth and measurements generated by finite-element analysis, black stars – detection results and reconstructed gradients using dipole approximation. (a) Positions for N=4 spheres. (b) Positions for N=4 cylinders. (c) Magnetic field intensity and gradients for spheres. (d) Magnetic field intensity and gradients for cylinders.

negative" dipoles concentrate in the four sub-regions that are the farthest to the measurement points. Obviously, by sampling other measurements in those four sub-regions, the number of "false negative" dipoles will decrease significantly and better detection performance can be achieved.

E. Verification of "High-wall" Effect

To verify the "high-wall" effect in the optimization, a case of N=5 is used to illustrate a closed circular trajectory of 17 measurement points, as shown in Fig. 16, where the small red circles represent the true dipoles, the red triangles represent the initial dipole candidates, and the black stars represent the converged dipole results. In the first scenario, three initial dipoles are put inside the measurement circle and the other six are outside. In the second situation, all the 9 initial dipoles are outside the measurement circle.

The optimization results in the first scenario successfully detect all true dipoles, while the second scenario estimates an incorrect number of true dipoles leading to a large location estimation error and multiple false positive. The true dipoles inside the measurement circle are entirely missed because no initial dipoles can cross the measurement circle. In real applications, if this kind of measurement scheme is inevitable, then sufficient number of initial dipole candidates shall be arranged in all separated sub-regions.

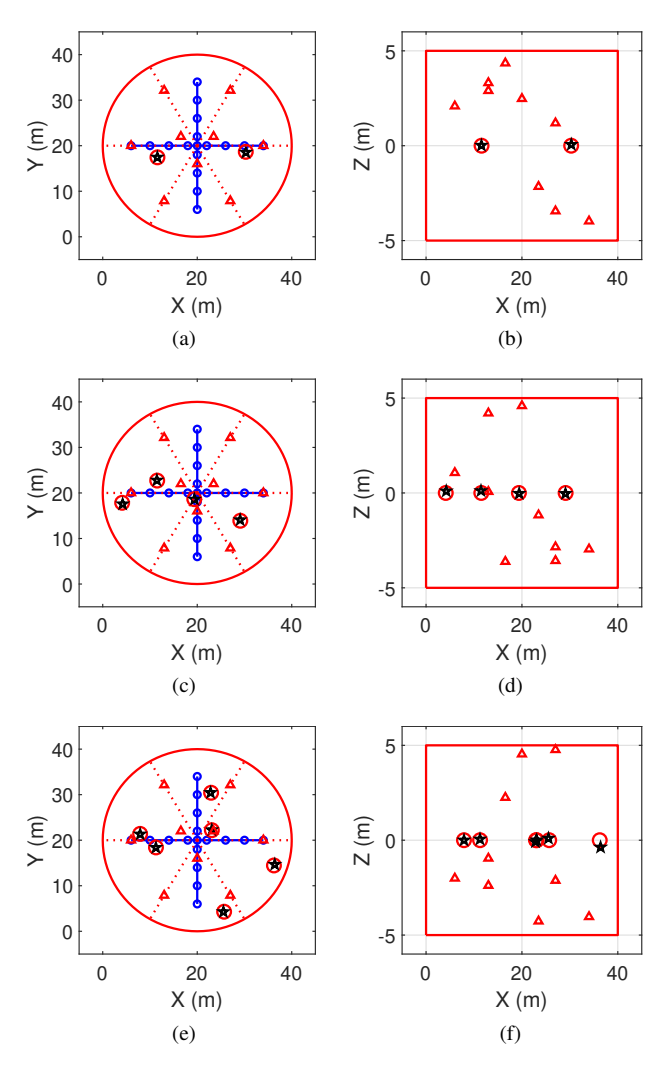


Fig. 14: Examples of good detection. The left column subfigures are projections on the X-Y plane, and the right column subfigures are projections on the X-Z plane. (a)-(b) N=2; (c)-(d) N=4; (e)-(f) N=6.

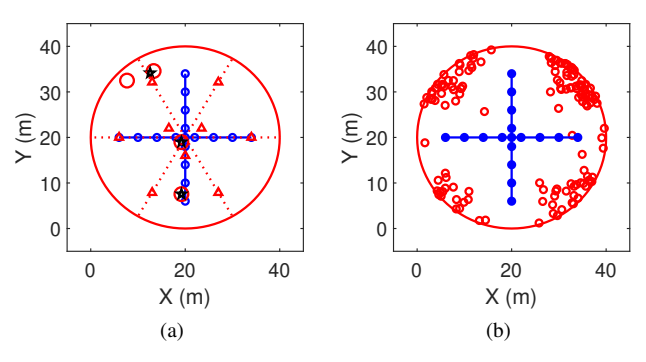


Fig. 15: Locations of "false negative" dipoles represented by small red circles: (a) An example for N=4 with initial dipole candidates represented by triangles; (b) Distribution of false negatives in 500 trials.

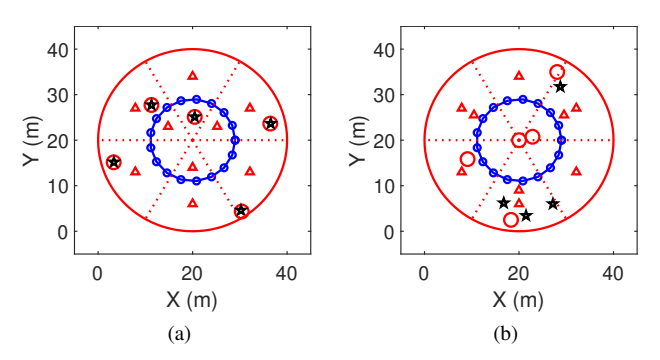


Fig. 16: Examples of the "high-wall" effect.

F. Comparison with Existing Methods

The performance of the proposed method is compared with the methods introduced in [23] and [22]. The simulation uses 500 trials of N=4 true dipoles randomly placed in the detection region. For the method of [23], 9 stations are used to make measurements and compute initial values for optimization. For the method of [22], the PSO uses 500 particles with their initial x, y, z randomly selected in [0, 40] m, [0, 40] m, and [-5, 5] m, respectively. The magnetic moments of each particle are given in [1000, 2000] Am² which is a more favorable condition. The clone hybrid algorithm is used for initialization. For the proposed method, we set $N_{\rm ini}=9,\,\alpha=0.03,\,\beta=0.5,\,Q=3.$ The initial moments are given in [0, 3000] Am². The SNRs of the measurements for three methods are all 49 dB. The results are shown in Tables V and VI. Note that the exact number of true dipoles is provided to the methods in [22] and [23], but no such information is fed to the proposed method.

TABLE V: COMPARISON of Precision, Recall AND Accuracy

Methods	Precision(%)	Recall(%)	Accuracy(%)
[23]	77.1	74.3	62.1
[22]	88.1	87.3	78.1
This paper	92.0	87.0	81.1

TABLE VI: COMPARISON OF POSITION ERRORS

Methods	$MRAE_{Px}(\%)$	$MRAE_{Py}(\%)$	$MRAE_{Pz}(\%)$
[23]	0.8355	0.9015	1.1310
[22]	0.4225	0.4426	0.4360
This paper	0.4175	0.4340	0.5045

The method of [23] performed the worst because it suffers from serious interference among target dipoles and the position estimates are poor. The performance of [22] is similar to the proposed method under the same noise level.

It should be noted that the PSO algorithm also requires proper initialization for the particles, especially when both the positions and moments are unknown and of quite different numerical levels. If the initial magnetic moments are set the same large range of $[0,3000]Am^2$ as that in the proposed method, the performance of [22] becomes much worse than the proposed method. Besides, the magnetic field \boldsymbol{B} usually suffer from higher level of noise than gradient data in same

scenarios. For example, the earth magnetic field is at the level of 10^4 nT, which is a serious noise source for measurement of \boldsymbol{B} . While the strength of earth magnetic gradient is usually lower than 10^{-1} nT/m.

V. CONCLUSION AND FUTURE WORKS

A novel joint optimization algorithm has been proposed for estimating the number of multiple magnetic dipole sources and their corresponding 3D locations and magnetic moments simultaneously. We initialize a large number of dipole candidates and introduce an indicator for each candidate and formulate a novel regularized mean square error cost function. We utilize the Levenberg-Marquardt (LM) algorithm and reinitialization to solve the nonlinear optimization. We have also discovered the "high-wall effect" related with the selections of measurement points and initial dipole candidates. Extensive simulations have demonstrated the outstanding performance of the proposed algorithm over existing methods. When the false alarm rate is set at 5×10^{-2} , the proposed algorithm achieves Recall of 0.91, 0.86, and 0.78 for the number of true dipoles being N=2,4,6, respectively. The performance is robust against external interference and parameter selections.

For future works, field experiments with a full tensor magnetic gradiometer are desirable, where the challenge is to integrate the measurement instruments using several 3-axis magnetometers. Alternatively, the proposed algorithm can be generalized to distributed detection and estimation when multiagent autonomous vehicles may be employed in a large area with a large number of targets.

ACKNOWLEDGMENT

This work of S. Chang and Y. Lin was supported by the National Natural Science Foundation of China under Grant 41906161. S. Chang was a visiting scholar at Lehigh University during Nov. 2019 - Jun. 2020. The work of Y. R. Zheng was supported in part by the US National Science Foundation under project CISE-1853257.

REFERENCES

- C. P. Du, M. Y. Xia, S. X. Huang, Z. H. Xu, X. Peng, and H. Guo, "Detection of a moving magnetic dipole target using multiple scalar magnetometers," *IEEE Geoscience and Remote Sensing Letters*, vol. 14, no. 7, pp. 1166–1170, July 2017.
- [2] S. Gürkan, M. Karapınar, and S. Doğan, "Detection and imaging of underground objects for distinguishing explosives by using a fluxgate sensor array," *Applied Sciences*, vol. 9, no. 24, p. 5415, 2019.
- [3] K.-M. Lee and M. Li, "Magnetic tensor sensor for gradient-based localization of ferrous object in geomagnetic field," *IEEE Trans. Magnetics*, vol. 52, no. 8, pp. 1–10, 2016.
- [4] C. Di Natali, M. Beccani, and P. Valdastri, "Real-time pose detection for magnetic medical devices," *IEEE Trans. Magnetics*, vol. 49, no. 7, pp. 3524–3527, 2013.
- [5] X. He, Z. Zheng, and C. Hu, "Magnetic localization and orientation of the capsule endoscope based on a random complex algorithm," *Medical devices (Auckland, NZ)*, vol. 8, p. 175, 2015.
- [6] J. Watermann and J. Lam, "Distributions of magnetic field variations, differences and residuals," SACLANT Undersea Research Centre, La Spezia (ITALY), Tech. Rep. SR-304, 1999.
- [7] A. Sheinker, A. Shkalim, N. Salomonski, B. Ginzburg, L. Frumkis, and B.-Z. Kaplan, "Processing of a scalar magnetometer signal contaminated by $1/f^{\alpha}$ noise," *Elsevier J. Sensors and Actuators A: Physical*, vol. 138, no. 1, pp. 105 111, 2007. [Online]. Available: http://www.sciencedirect.com/science/article/pii/S0924424707003214

- [8] N. Ahmed, A. Radchenko, D. Pommerenke, and Y. R. Zheng, "Design and evaluation of low-cost and energy-efficient magneto-inductive sensor nodes for wireless sensor networks," *IEEE Systems Journal*, vol. 13, no. 2, pp. 1135–1144, 2019.
- [9] H. Huang and Y. R. Zheng, "3-D localization of wireless sensor nodes using near-field magnetic-induction communications," *Elsevier Physical Communication*, vol. 30, pp. 97 – 106, 2018. [Online]. Available: http://www.sciencedirect.com/science/article/pii/S187449071730160X
- [10] T. Yoshii, "Method for detecting a magnetic source by measuring the magnetic field thereabout," Jan. 5 1982, US Patent 4,309,659.
- [11] W. Wynn, "Magnetic dipole localization with a gradiometer: Obtaining unique solutions," in IGARSS'97. 1997 IEEE International Geoscience and Remote Sensing Symposium Proceedings. Remote Sensing-A Scientific Vision for Sustainable Development, vol. 4, 1997, pp. 1483–1485.
- [12] P. J. Heath, "Analysis of potential field gradient tensor data: forward modelling, inversion and near-surface exploration," Ph.D. dissertation, School of Chemistry and Physics, the University of Adelaide, 2007.
- [13] A. Reid, J. Allsop, H. Granser, A. Millett, and I. Somerton, "Magnetic interpretation in three dimensions using euler deconvolution," *Geo*physics, vol. 55, no. 1, pp. 80–91, 1990.
- [14] C. Zhang, M. F. Mushayandebvu, A. B. Reid, J. D. Fairhead, and M. E. Odegard, "Euler deconvolution of gravity tensor gradient data," *Geophysics*, vol. 65, no. 2, pp. 512–520, 2000.
- [15] G. R. Cooper and R. C. Whitehead, "Determining the distance to magnetic sources," *Geophysics*, vol. 81, no. 2, pp. J25–J34, 2016.
- [16] J. Almaguer, H. Lopez-Loera, J. L. Macias, R. Saucedo, V. Yutsis, and R. Guevara, "Geophysical modeling of La Primavera caldera and its relation to volcanology activity based on 3D susceptibility inversion and potential data analysis," *Elsevier Journal of Volcanology and Geothermal Research*, vol. 393, p. 106556, 2020. [Online]. Available: http://www.sciencedirect.com/science/article/pii/S0377027318304062
- [17] F. C. Teixeira and A. Pascoal, "Magnetic navigation and tracking of underwater vehicles," *Elsevier IFAC Proceedings Volumes*, vol. 46, no. 33, pp. 239–244, 2013.
- [18] R. Hansen and L. Suciu, "Multiple-source Euler deconvolution," Geophysics, vol. 67, no. 2, pp. 525–535, 2002.
- [19] C. C. Ku and J. A. Sharp, "Werner deconvolution for automated magnetic interpretation and its refinement using Marquardt's inverse modeling," *Geophysics*, vol. 48, no. 6, pp. 754–774, 1983.
- [20] R. Hansen, "3D multiple-source werner deconvolution for magnetic data," *Geophysics*, vol. 70, no. 5, pp. L45–L51, 2005.
- [21] S. Song, C. Hu, and M. Q.-H. Meng, "Multiple objects positioning and identification method based on magnetic localization system," *IEEE Transactions on Magnetics*, vol. 52, no. 10, pp. 1–4, 2016.
- [22] C. Hu, M. Li, M. Q.-H. Meng, S. Song et al., "A new tracking system for three magnetic objectives," *IEEE Trans. Magnetics*, vol. 46, no. 12, pp. 4023–4029, 2010.
- [23] S. Hu, J. Tang, Z. Ren, C. Chen, C. Zhou, X. Xiao, and T. Zhao, "Multiple underwater objects localization with magnetic gradiometry," *IEEE Geoscience and Remote Sensing Letters*, vol. 16, no. 2, pp. 296–300, 2018.
- [24] J. J. Moré, "The levenberg-marquardt algorithm: Implementation and theory," in *Numerical Analysis*, G. A. Watson, Ed. Berlin, Heidelberg: Springer Berlin Heidelberg, 1978, pp. 105–116.
- [25] D. I. Oléan, J. G. Perović, B. M. Kolundžija, and A. R. Djordjević, "Recent advances in entire-domain analysis of 2-d structures using method of moments," in 2019 International Conference on Electromagnetics in Advanced Applications (ICEAA), 2019, pp. 1111–1115.

Shuai Chang received the B.S. degree in automation and the Ph.D degree in navigation, guidance and control, from Harbin Engineering University, Harbin, Heilongjiang Province, China, in 2010 and 2015, respectively. Since 2015, Dr. Chang has been an assistant professor in the College of Marine Science and technology at Tianjin University, Tianjin, China. He was a visiting scholar at Lehigh University during Nov. 2019 - Jun. 2020. His research interests include magnetic source detection and geophysical field aided navigation.

Ye Lin received her B.S. degree in marine resources development technology from Dalian University of Technology, Dalian, Liaoning Province, China, in 2019. She is currently a master student in marine science at Tianjin University. Her research interests include marine magnetic source detection and underwater SLAM.

Yahong Rosa Zheng (M'03-SM'07-F'15) received the B.S. degree in electrical engineering from the University of Electronic Science and Technology of China, Chengdu, China, in 1987, the M.S. degree in electrical engineering from Tsinghua University, Beijing, China, in 1989, and the Ph.D. degree in electrical engineering from Carleton University, Ottawa, ONT, Canada, in 2002. From 1989 to 1996, she was an engineer and a technical staff at several companies, including Beijing Peony Electronics Group, Beijing, China, Sagem Australasia, Sydney, NSW, Australia, and Polytronics, Markham, ONT, Canada. From 2003 to 2005, she was an NSERC Postdoctoral Fellow with the University of Missouri-Columbia. From 2005 to 2018, she was a faculty member with Missouri University of Science and Technology, Rolla, MO, USA, where she was Wilkens Missouri Telecommunications Chair Professor in 2017-2018. Since 2018, she is a professor at Lehigh University, Bethlehem, PA, USA. Her research interests include underwater cyber-physical systems, real-time embedded systems and signal processing, wireless communications, and wireless sensor networks.

Dr. Zheng served as an Associate Editor for IEEE Transactions on Wireless Communications 2006-2008 and IEEE Transactions on Vehicular Technology 2008-2016. She has been Associate Editor for the IEEE Journal of Oceanic Engineering since 2016. She is the recipient of an NSF CAREER award in 2009. Since 2015, she has been IEEE Fellow and a Distinguished Lecturer for the IEEE Vehicular Technology Society.

Xiaomei Fu received the M.S. and the Ph.D. degree from Tianjin University, China in 2000 and 2006, respectively. She was a visiting scholar at the Imperial College of London, UK from 2009 to 2010. Dr. Fu is currently a professor at Tianjin University, China. Her research interests include wireless network communication, physical layer security, and underwater communication networks.